ADVANCED OPTICAL MATERIALS
www.advopticalmat.de

Magneto-Optical Bi-Substituted Yttrium and Terbium Iron Garnets for On-Chip Crystallization via Microheaters

Kensuke Hayashi, Khoi Phuong Dao, Miela J. Gross, Luigi Ranno, Jia Xu Brian Sia, Takian Fakhrul, Qingyang Du, Nilanjan Chatterjee, Juejun Hu, and Caroline A. Ross**

Ferrimagnetic iron garnets enable magnetic and magneto-optical functionality in silicon photonics and electronics. However, garnets require high-temperature processing for crystallization which can degrade other devices on the wafer. Here bismuth-substituted yttrium and terbium iron garnet (Bi-YIG and Bi-TbIG) films are demonstrated with good magneto-optical performance and perpendicular magnetic anisotropy (PMA) crystallized by a microheater built on a Si chip or by rapid thermal annealing. The Bi-TbIG film crystallizes on Si at 873 K without a seed layer and exhibits good magneto-optical properties with Faraday rotation (FR) of −1700 deg cm^{-1}. The Bi-YIG film also crystallizes on Si and fused SiO_2 at 873 K without a seed layer. Rapidly cooled films exhibit PMA due to the tensile stress caused by the thermal expansion mismatch with the substrates, increasing the magnetoelastic anisotropy by 4 kJ m^{-3} versus slow-cooled films. Annealing in the air for 15 s using the microheater yields fully crystallized Bi-TbIG on the Si chip.

1. Introduction

Silicon photonics, which integrates elements such as optical waveguides, optical switches, optical modulators, and photodetectors on silicon substrates, combines the advantages of optical communications (high-speed signal transmission, wide bandwidth, and low power) with the controllability of CMOS-based electronics.[1,2] Optical elements in silicon photonics operating at the 1550 nm communication wavelength are often built on Si-on-insulator (SOI) substrates.[1,2] Since the infrared light is also generated using lasers integrated onto the same substrate, a complete photonic integrated circuit requires integrated optical isolators to control the flow of light.[3,4] Magneto-optical phenomena can provide the necessary nonreciprocal mode conversion or phase shift to enable optical isolation, and a number of isolators have been developed using iron garnets (IGs) with good magneto-optical figures of merit.[3–10] Iron garnets have a composition of $A_3(Fe,X)_5O_{12}$ where A is Y, Bi, or rare earth (RE) such as Tb, Ce, Eu, Dy, etc., and X represents substitutions on the Fe sites. Iron garnets are ferrimagnets, with the A cations occupying dodecahedral sites and Fe occupying octahedral and tetrahedral sites coupled antiferromagnetically via superexchange.[11] Bi and Ce substitutions into $Y_3Fe_5O_{12}$ and $Tb_3Fe_5O_{12}$ are particularly advantageous for achieving good magneto-optical properties at wavelengths near 1550 nm.[5–10,12–15]

Faraday rotation (FR) of −400–−2000 deg cm^{-1} has been reported in Bi-substituted $Y_3Fe_5O_{12}$ (Bi-YIG),[4,9,12,13] and −500–6200 deg cm^{-1} in Bi-substituted $Tb_3Fe_5O_{12}$ (Bi-TbIG).[7,14] Bi substitution not only improves FR, but also lowers the crystallization temperature of IG garnets[16–18] and plays a major role in crystallizing the garnets by post-growth annealing.

K. Hayashi, K. P. Dao, L. Ranno, J. X. B. Sia, T. Fakhrul, J. Hu, C. A. Ross
Department of Materials Science and Engineering
Massachusetts Institute of Technology
Cambridge, MA 02139, USA
E-mail: hayashik@mit.edu; caross@mit.edu

M. J. Gross
Department of Electrical Engineering and Computer Science
Massachusetts Institute of Technology
Cambridge, MA 02139, USA

The ORCID identification number(s) for the author(s) of this article can be found under https://doi.org/10.1002/adom.202400708

DOI: 10.1002/adom.202400708

J. X. B. Sia
School of Electrical and Electronic Engineering
Nanyang Technological University
Singapore 639798, Singapore

T. Fakhrul
Bangladesh University of Engineering and Technology (BUET)
Dhaka 1000, Bangladesh

Q. Du
Research Center for Intelligent Optoelectronic Computing
Zhejiang Laboratory
Hangzhou, Zhejiang 311100, China

N. Chatterjee
Department of Earth, Atmospheric and Planetary Sciences
Massachusetts Institute of Technology
Cambridge, MA 02139, USA

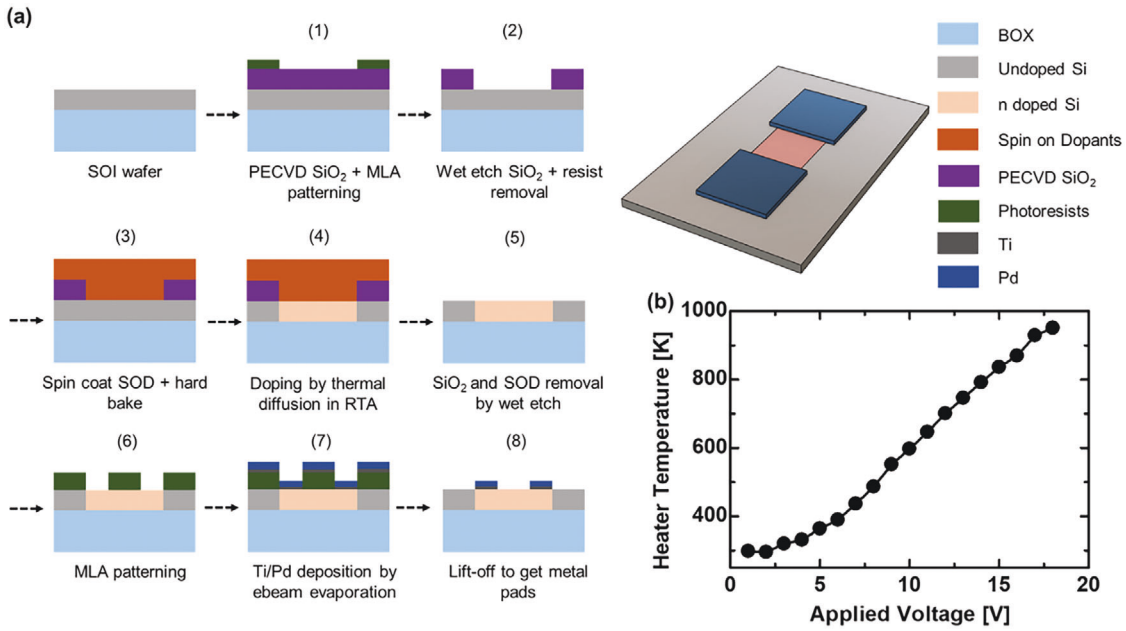

Figure 1. Integrated micro-heater fabricated on silicon on insulator (SOI) platform. a) Heater schematic and fabrication process. BOX: buried oxide; PECVD: plasma-enhanced chemical vapor deposition; SOD: spin-on dopants; MLA: maskless aligner. b) Heater performance: steady state temperature versus applied voltage.

IG-based isolators have been made by monolithic integration,[4,5,7,9,10] in which the IG is formed directly on the SOI, for example as a cladding layer on the Si waveguide, or by heterogeneous integration,[4,6,8] in which the IG is fabricated separately and bonded onto the SOI. Monolithic integration provides superior scalability and compatibility with a range of device designs,[4] but the process requires a high thermal budget, and the performance of IG thin films is generally poorer than that of the single-crystalline films used in heterogeneous integration. As-grown IG films on non-garnet substrates are typically amorphous and require post-growth annealing to produce a polycrystalline film, in some cases using a seed layer of another garnet.[4] There are several reports of IG crystallization on Si substrates using YIG and $Gd_3Ga_5O_{12}$ (GGG) seed layers,[5,9,19] as well as seed-layer-free growth of TbIG, EuIG, and DyIG on Si substrates.[7,10,14,15,20,21] In addition, the fabrication of TbIG-based isolators without a seed layer has also been reported.[7,10] The annealing temperature was 1073 K to crystallize Bi-substituted YIG (Bi-YIG) on or under a YIG seed layer,[9] and 1173 K for TbIG without a seed layer,[7,10,14,15] which is well above the maximum backend CMOS processing temperature.[22,23] Hence, crystallization of garnet on CMOS requires approaches other than heating the entire substrate. Localized annealing may be used to heat only the desired area, for example by using laser annealing[24,25] over areas of a few μm^2. However, the small laser spot size and limited scan rate reduce the applicability of this technique to small areas.

In addition to its magneto-optical properties, Bi-YIG is a promising material for spintronics applications[26,27] due to its low damping and fast magnetization dynamics. Bi-YIG with PMA is favorable for spin orbit torque-driven switching,[26,27] and PMA can be promoted by magnetoelastic anisotropy resulting from a tensile in-plane strain state combined with the negative magnetostriction[26,28] of Bi-YIG. Integration of Bi-YIG on non-garnet substrates allows for the manipulation of the strain state via thermal expansion mismatch with the substrate[20] or via piezoelectric strain,[29] thereby providing additional methods to control the magnetic anisotropy.

Here, we propose local crystallization of garnet films using a micro-heater built into a Si substrate.[30] **Figure 1** shows the process for making the micro-heater. The microheater is composed of a Si square pattern whose resistance is adjusted by dopant concentration, allowing local annealing by resistance heating. The shape and size of the heater and the current flow provide control over the temperature, which can exceed 1100 K, and the temperature profile. (After use, the microheater remains on the photonic device, and its effects on device performance should be considered.) To develop magneto-optical and spintronic garnets that can be crystallized using the heater, we first investigate the effects of composition parameters Bi% = {Bi/(Bi + Tb or Y)} × 100 and R = {(Bi + Tb or Y)/Fe} on the crystallization temperature and the magnetic and magneto-optical properties of both Bi-TbIG and Bi-YIG prepared by pulsed laser deposition (PLD) on Si substrates, using rapid thermal annealing (RTA) in air. For compatibility with the on-chip heater, all films were deposited at room temperature which enables lift-off processing with photoresist, and crystallization of the films was performed in air rather than under oxygen. We show that Bi-TbIG films on Si substrates crystallize at lower annealing temperatures than TbIG while displaying good magneto-optical properties. Furthermore, Bi-YIG films on Si or fused SiO_2 substrates prepared by co-deposition of YIG with BiIG or $BiFeO_3$ (BFO) demonstrated PMA after rapid cooling due to thermal expansion mismatch with the substrates. We finally demonstrate on-chip crystallization of the Bi-TbIG films by local annealing using the micro-heaters.

2. Results and Discussion

2.1. Crystallization and Microstructure of the Bi-TbIG and Bi-YIG Films

Bi-TbIG and Bi-YIG films with a range of Bi content were grown on Si at room temperature by co-deposition from BiIG and TbIG or YIG targets (**Table 1**). Cation composition was measured by wavelength dispersive spectrometry (WDS) (Experimental Section). Most films had thicknesses of 150–200 nm but the TbIG film with Bi% = 0 was grown thicker to facilitate magnetic analysis since its saturation magnetization M_S is low at room temperature.[11] The films were annealed by RTA at various temperatures in air for 200 s and the resulting crystal phases were assessed by XRD (Section S1, Supporting Information). **Figure 2**a,d shows the effect of annealing temperature and Bi content on phase formation for the Bi-TbIG and Bi-YIG films. Circle symbols (○) indicate that only garnet phase was observed in the XRD patterns, × indicates garnet plus another phase, and ▲ indicates an amorphous state without XRD peaks. Bi lowers the crystallization temperature as reported in prior studies,[16–18] but above ≈50% substitution of Bi for Y or Tb, non-garnet phases form. These results are consistent with prior works,[7,16–18,31,32] which have shown that it is challenging to incorporate Bi% > 50 into YIG without using epitaxial growth on a garnet substrate or seed layer due to the instability of the BiIG garnet phase. Both the Bi-TbIG and Bi-YIG films made in this study crystallize below 973 K, which can be reached with the microheater. In addition to the Bi-TbIG and Bi-YIG films, a BiIG film was grown epitaxially on a (111) GGG substrate at 833 K as a reference sample, without a post-growth anneal.

Table 1. Sample information.

Bi-TbIG on Si made with TbIG and BiIG targets

Cation composition	Bi%	R	Thickness [nm]	Crystallization conditions
$Tb_{2.78}Fe_5O_x$	0	0.56	400 ± 20	1173 K for 200 s in RTA
$Bi_{0.50}Tb_{2.96}Fe_5O_x$	14	0.69	180 ± 10	973 K for 200 s in RTA
$Bi_{1.20}Tb_{2.21}Fe_5O_x$	35	0.68	170 ± 20	973 K for 200 s in RTA
$Bi_{1.31}Tb_{1.88}Fe_5O_x$	41	0.64	160 ± 10	873 K for 200 s in RTA
$Bi_{1.75}Tb_{1.63}Fe_5O_x$	48	0.68	162 ± 9	873 K for 200 s in RTA
$Bi_{2.24}Tb_{1.31}Fe_5O_x$	63	0.71	150 ± 5	873 K for 200 s in RTA

Bi-YIG on Si made with YIG and BiIG targets

Cation composition	Bi%	R	Thickness [nm]	Crystallization conditions
$Y_{2.55}Fe_5O_x$	0	0.51	140 ± 10	1073 K for 200 s in RTA
$Bi_{0.44}Y_{2.23}Fe_5O_x$	16	0.53	130 ± 10	1023 K for 200 s in RTA
$Bi_{0.85}Y_{1.89}Fe_5O_x$	31	0.55	150 ± 5	973 K for 200 s in RTA
$Bi_{1.17}Y_{1.60}Fe_5O_x$	42	0.55	157 ± 9	973 K for 200 s in RTA
$Bi_{1.33}Y_{1.51}Fe_5O_x$	47	0.57	147 ± 6	973 K for 200 s in RTA
$Bi_{1.75}Y_{1.12}Fe_5O_x$	59	0.57	157 ± 8	923 K for 200 s in RTA

BiIG on GGG made with BiIG target

Nominal Composition	Method	Thickness [nm]	Crystallization conditions
$Bi_3Fe_5O_{12}$	Epitaxial	160 ± 10	None (833 K growth)

Bi-YIG with Bi% = 60 and R = 0.71 made with YIG and BFO targets

Cation composition	Substrate	Thickness [nm]	Crystallization conditions
$Bi_{2.13}Y_{1.40}Fe_5O_x$	Si	205 ± 14	873 K for 10 h, furnace
$Bi_{2.13}Y_{1.40}Fe_5O_x$	Si	45 ± 1	873 K for 3d w/wo quench
$Bi_{2.13}Y_{1.40}Fe_5O_x$	Fused SiO_2	45 ± 1	873 K for 3d w/wo quench

Composition, thickness, substrate, and crystallization conditions for the garnet films. The oxygen content was not measured. R = (Bi + Tb or Y)/Fe = 0.6 for ideal garnet stoichiometry.

Figure 2b,c,e,f shows the XRD patterns and out-of-plane lattice parameters of single-phase garnet samples. The out-of-plane lattice parameter increases with increasing Bi% due to the larger ionic radius of Bi^{3+} compared to Tb^{3+} and Y^{3+} (Section S2, Supporting Information). However, the lattice parameter of the films with Bi% = 0, i.e., TbIG (1.239(0) nm) and YIG (1.232(3) nm) is 0.3–0.4% smaller than that of powder samples reported in previous studies: TbIG (1.24339(1) nm)[33] and YIG (1.23774(2) nm).[34] Furthermore, the lattice parameter of our Bi-YIG is smaller than that of powders with the same Bi%.[16] The lower out-of-plane lattice parameter is consistent with a tensile strain in the films which arises from thermal expansion mismatch with Si.[20,21] The thermal expansion coefficient (TEC) of iron garnets (TbIG: 10.2 10^{-6} K^{-1},[35] YIG: 10.2 10^{-6} K^{-1},[35] BiIG: 12.9 10^{-6} K^{-1}[35]) is larger than that of Si (2.6 10^{-6} K^{-1},[36]) which would lead to an in-plane elastic tensile strain of ≈0.5% on cooling (neglecting strain relaxation) and a corresponding reduction in the out-of-plane lattice parameter.

Figure 3 shows SEM images, AFM images, electron backscatter diffraction (EBSD) crystalline orientation mapping, and EBSD intensity mapping of a Bi-TbIG film with Bi% = 48 annealed at 873 K and a Bi-YIG film with Bi% = 47 annealed at 973 K. The Bi-TbIG film shows equiaxed grains characteristic of nucleation and growth to impingement, with a random crystalline orientation. The Bi-YIG film shows a similar grain structure but radial linear features are observed within the grains and the crystal orientation within the grain is less well defined. By analogy with DyIG films on Si[21] the radiating features represent low angle grain boundaries which occur as the interface between the rapidly growing crystal and the amorphous region becomes unstable. Impingement of the grains then leads to rougher grain boundaries than in the case of Bi-TbIG. Section S3 (Supporting Information) shows SEM, AFM, and EBSD data for other samples with a range of Bi%. The instability of the crystallization front and the low angle grain boundaries are only prominent for the Bi-YIG with Bi% = 47; other Bi-YIG samples have straight grain boundaries and no obvious radial features.

The R-value parameterizes the ratio of Bi, Tb, and Y to Fe, and R = 0.6 in an ideal garnet. According to WDS analysis, the Bi-TbIG films were Fe-deficient whereas the Bi-YIG had excess Fe (Table 1). The deviation of the film composition from that of the target is a result of differential scattering of species in the plume and/or the volatility of Bi, and depends on growth

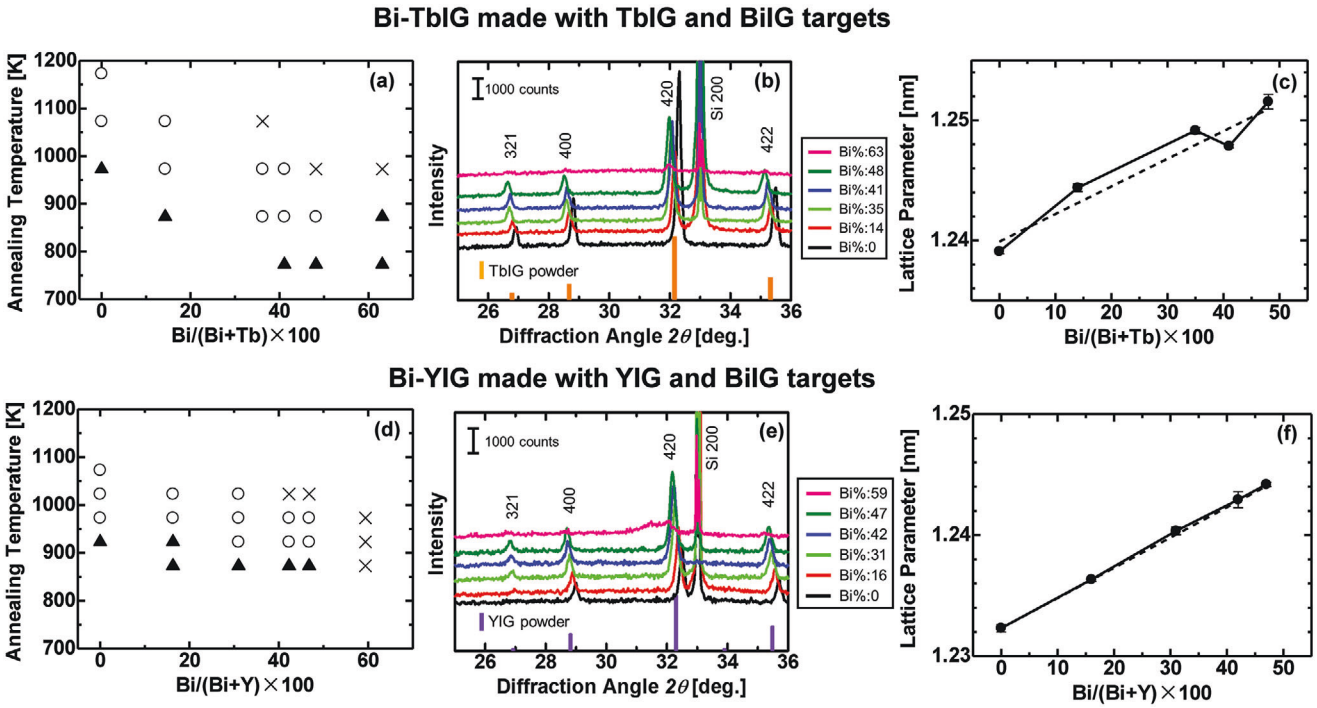

Figure 2. a,d) Crystallization of the Bi-TbIG and Bi-YIG films. Circle symbols (°) indicate that only garnet phase was observed in the XRD patterns, × indicates garnet plus another phase, and ▲ indicates an amorphous state without XRD peaks. b,e) XRD patterns compared to the powder diffraction files of garnets (TbIG[33] and YIG[34]) and c,f) out-of-plane lattice parameter with a linear fit (dotted line).

conditions such as oxygen pressure and substrate temperature. To investigate the effect of R on the crystallization of iron garnet, additional Bi-YIG films were made by co-deposition from the YIG target and a $BiFeO_3$ (BFO) target, leading to Bi% = 60 and R = 0.71 (composition $Bi_{2.13}Y_{1.40}Fe_5O_x$). Thicknesses of 24, 45, 62, 205, and 223 nm were prepared on Si as well as a 45 nm thick film on fused SiO_2 (Table 1; Table S1, Supporting Information). Increasing the R value, i.e., introducing a Fe deficiency, stabilized the garnet structure even at Bi% = 60 (**Figure** 4a; Section S4, Supporting Information). Crystallization into the garnet phase

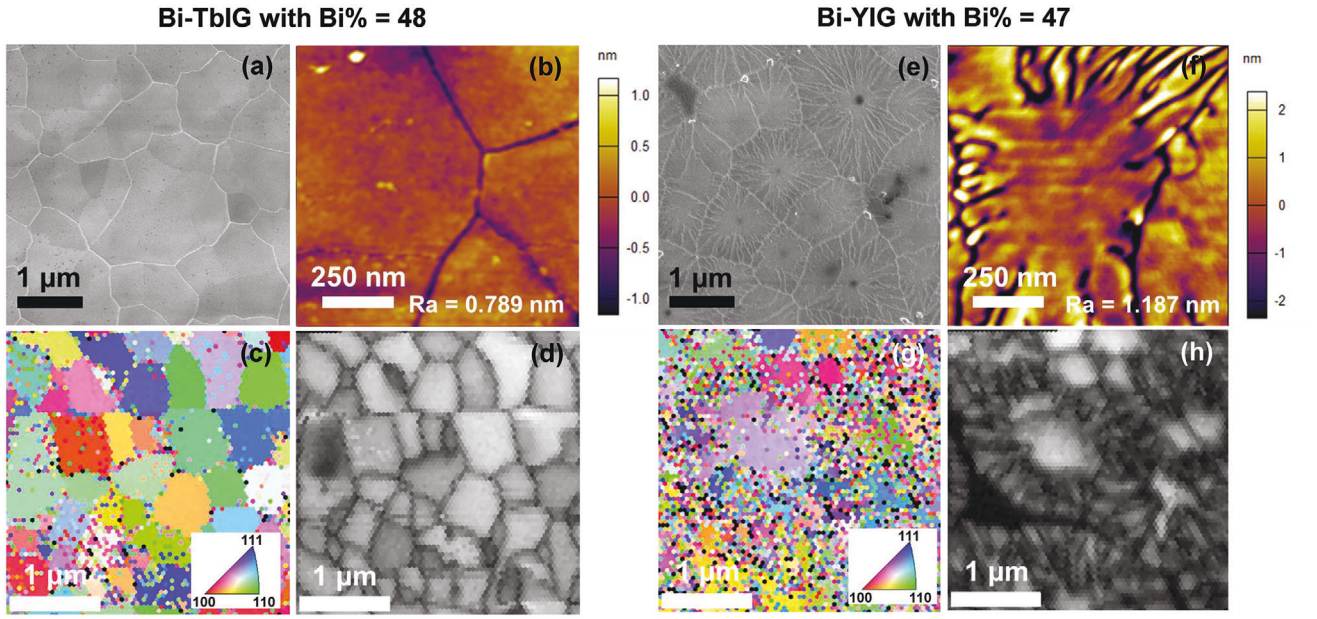

Figure 3. a,e) SEM image, b,f) AFM image, c,g) EBSD crystalline orientation mapping, and d,h) EBSD intensity mapping of the Bi-TbIG film with Bi% = 48 and the Bi-YIG film with Bi% = 47 in Table 1. In panel (d,h), the brightness of the pixels represents the diffraction intensity.

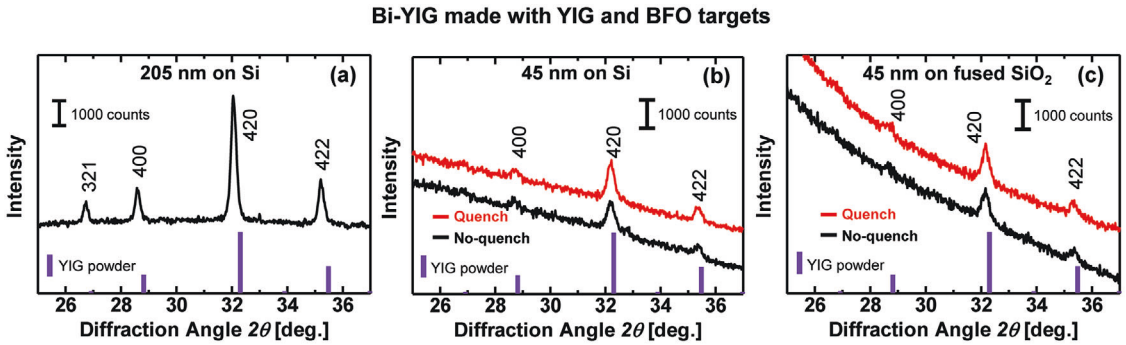

Figure 4. XRD patterns of a) the 205 nm thick Bi-YIG film on Si, b) the 45 nm thick Bi-YIG films on Si with/without quench, and c) the 45 nm thick Bi-YIG films on fused SiO_2 with/without quench.

was obtained at temperatures as low as 873 K for the 205 nm thick film, lower than the temperatures shown in Figure 2d. From Figure 4a, the high R value leads to a higher out-of-plane lattice parameter than that extrapolated from Figure 2f for Bi% = 60, i.e., 1.249(1) nm versus 1.2476 nm. The out-of-plane lattice parameter increase is due to a reduction in the in-plane tensile thermal mismatch stress, and by the increase in unit cell volume due to occupancy of the octahedral Fe sites by excess Bi and Y.

The effects of annealing temperature, annealing time, and film thickness on crystallization are described in Section S4, (Supporting Information). For a fixed composition, the extent of crystallization of Bi-YIG is reduced as the film thickness decreases. For example, after 923 K–200 s annealing, the 223 nm thick film is fully crystallized whereas a 62 nm thick film consists of circular crystallized regions within an amorphous film (Figures S9 and S10, Supporting Information). This suggests a larger number of nucleation sites are present within a thicker film. Figure S11 (Supporting Information) shows that 45 nm films are over 90% crystallized after 3 days at 873 K, whereas 24 nm thick films were only partly crystallized after 2 weeks at 873 K.

Figure 4b,c compares the XRD of 45 nm films grown on Si and fused SiO_2, for both slow (unquenched, black) and fast (quenched, red) cooling from the annealing temperature. The lattice parameters are similar for all four samples within the measurement accuracy (1.24(3) nm and 1.243(8) nm for Bi-YIG/Si with and without quenching; 1.24(2) nm and 1.243(8) nm for Bi-YIG/SiO_2 with and without quenching) but the Bi-YIG/SiO_2 is expected to have greater in-plane tensile strain due the larger thermal expansion mismatch with the substrate (TEC for fused SiO_2: 0.5×10^{-6} K^{-1}.[37]) The effect of thermal mismatch strain on anisotropy is discussed below.

2.2. Magnetic Properties of the Bi-TbIG and Bi-YIG Films

Figure 5a,b,d,e shows in-plane and out-of-plane magnetic hysteresis loops at room temperature for the Bi-TbIG and Bi-YIG films grown from the BiIG and TbIG or YIG targets. The in-plane direction is the easy axis for all the samples but the magnetic anisotropy changes with Bi%. The Bi% dependence of the M_S and the magnetoelastic anisotropy K_{ME}, which is calculated from the area between the in-plane and out-of-plane magnetic hysteresis loops, are shown in Figure 5c,f. As the TbIG without Bi does not saturate at 1 T, the in-plane magnetization at 1 T is used as M_S.

For the Bi-YIG films, M_S is ≈120 kA m^{-1}, almost independent of Bi%, but with a small decrease at high Bi% which may result from incomplete crystallization. In contrast, Bi-TbIG films show a dependence of M_S on composition. This can be understood from the Bi-dependent compensation temperature T_{comp} of Bi-TbIG.[11] The M_S of a REIG is the difference between the tetrahedral Fe and (octahedral Fe plus dodecahedral RE) sublattice magnetizations, i.e., $M_S = |M_{dod} + M_{oct} - M_{tet}|$. In TbIG, replacing Tb^{3+} with nonmagnetic Bi^{3+} lowers M_{dod} and hence lowers T_{comp}, which is below room temperature. This raises the room temperature M_S as observed in Figure 5f and in prior works.[15,19] To investigate T_{comp} for the Bi-TbIG films, M–H loops were measured from 123 K to 298 K for each Bi%, and T_{comp} is identified as the temperature where the magnetization is lowest. The M–H loops of the Bi-TbIG films near T_{comp} and the dependence of the T_{comp} on Bi% are shown in Section S5 (Supporting Information). T_{comp} of the TbIG film with Bi% = 0 is 260 ± 13 K, close to the bulk value of 246 K,[11] and decreases to below 123 K with increasing Bi%.

The total anisotropy of the films K_{tot} was obtained from the area difference between the anhysteretic loops up to saturation in the in-plane and out-of-plane directions from Figure 5a,b,d,e.[20] The hysteresis was first subtracted to produce the anhysteretic loops by averaging the ascending and descending loops, and the out-of-plane loop was normalized to the saturation magnetization of the in-plane loop. In the total magnetic anisotropy K_{tot} of for randomly oriented polycrystalline IG films, there is no net magnetocrystalline anisotropy, and we assume there is no growth-induced anisotropy because the films were annealed after growth. In addition, any interfacial anisotropy is neglected due to the large film thickness. Thus, $K_{tot} = K_S + K_{ME}$, where K_S is the shape anisotropy given by $K_S = -\mu_0 M_S^2/2$, K_{ME} is the magnetoelastic anisotropy, and μ_0 is the vacuum permeability. For a polycrystalline film under a biaxial stress, $K_{ME} = \frac{-3}{2(1-\nu)} \lambda E(\epsilon_{//} - \epsilon_{\perp})$ with the Poisson's ratio ν, magnetostriction λ, Young's modulus E, and in-plane and out-of-plane strains $\epsilon_{//}$ and $\epsilon_{\perp}$. In addition, the magnetostriction λ of a polycrystalline cubic material is related to its magnetoelastic coefficients λ_{100} and λ_{111} according to

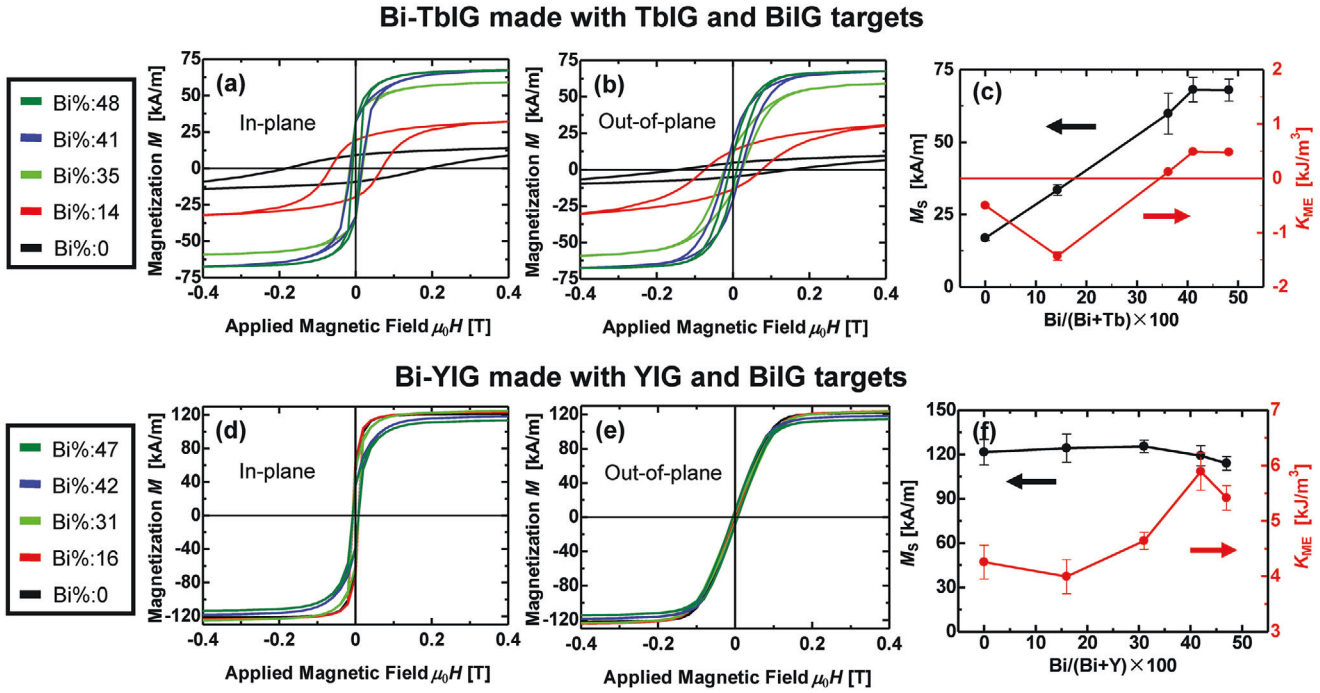

Figure 5. Room temperature in-plane and out-of-plane *M–H* loops of a,b) Bi-TbIG films, and d,e) Bi-YIG films. Bi% dependence of M_S and K_{ME} for c) Bi-TbIG films and f) Bi-YIG films.

$\lambda = \frac{2}{5}\lambda_{100} + \frac{3}{5}\lambda_{111}$, thus λ can be calculated from the λ_{100} and λ_{111} values of single crystals.

For Bi-TbIG, K_{ME} is negative at Bi% < 35 and positive at Bi% ≥ 35. This is attributed to the dependence of the magnetostriction on Bi content. The magnetostriction of polycrystalline TbIG (Bi% = 0) at room temperature is positive, 5.9×10^{-6},[38] and in combination with the tensile stress leads to a negative K_{ME} promoting an in-plane easy axis in the TbIG film. On the other hand, Bi addition contributes a negative magnetostriction which has been extrapolated as -3.3×10^{-6} for polycrystalline BiIG,[28] implying a sign change for λ as Bi is added to TbIG. In contrast, the magnetostriction coefficient of polycrystalline YIG is negative, $\lambda = -2.1 \times 10^{-6}$ [38] and Bi addition increases its magnitude without changing the sign. K_{ME} of the Bi-YIG films is therefore positive for all compositions, increasing with Bi% as observed in Figure 5f. The positive K_{ME} favors PMA, but is smaller than the shape anisotropy ($K_S = 9.0$ kJ m^{-3} for $M_S = 120$ kA m^{-1}) and the films have an in-plane easy axis.

We estimate the magnitude of K_{ME} from the stress and the magnetostriction coefficient. The in-plane strain $\epsilon_{//}$ caused by a thermal expansion mismatch is given by the product of the temperature change ΔT from the annealing temperature to room temperature and the difference between the thermal expansion coefficients of the film and substrate $\Delta\alpha$, i.e., $\epsilon_{//} = \Delta\alpha\Delta T$. $\epsilon_{\perp} = -2\nu\epsilon_{//}/(1-\nu)$ with ν the Poisson ratio of the film. Considering the Bi-YIG/Si with Bi% = 47 cooled from 873 to 300 K, taking $\Delta a = 8.9\times 10^{-6}$ K^{-1}, $\lambda = -2.7 \times 10^{-6}$, $E = 205$ GPa,[28] and $\nu = 0.30$[28] yields K_{ME} of 11.2 kJ m^{-3}. This suggests that K_{ME} can exceed K_S. However, the measured $K_{ME} = 5.4 \pm 0.2$ kJ m^{-3} is smaller, likely due to strain relaxation during the cooling after the anneal.

Figure 6a shows in-plane and out-of-plane magnetic hysteresis loops at room temperature for the 205 nm thick Bi-YIG films with Bi% = 60 and R = 0.71 made from the YIG and BFO targets. The M_S of the Bi-YIG film is ≈120 kA m^{-1}, similar to other Bi-YIG films which indicates that the film is well crystallized after the long-duration annealing (10 hours). However, the K_{ME} is 4.0 ± 0.3 kJ m$-^3$, which is smaller than that of the high-Bi% YIG films annealed by RTA. The lower K_{ME} is attributed to the slow cooling rate (1 K min^{-1}) in the furnace after crystallization, which promotes strain relief of the film. Figure 6b,c and Figure S12a,b (Supporting Information) show hysteresis loops for the 45 nm Bi-YIG film on Si or fused SiO_2 that was quenched after crystallization. The M_S of both films is ≈110 kA m^{-1} yielding K_S = 7.6 kJ m^{-3} and the K_{ME} is 8.0 ± 0.2 and 8.6 ± 0.2 kJ m^{-3}, respectively. In both samples, the out-of-plane loop saturated first, consistent with the film having PMA. Furthermore, the Bi-YIG film on fused SiO_2 shows stronger PMA consistent with its ≈8% higher in-plane strain due to the greater thermal expansion mismatch between Bi-YIG and fused SiO_2.

Polar magneto-optical Kerr effect (P-MOKE) images of the 45 nm thick Bi-YIG film on Si are shown in Figure 6d and Figure S12c (Supporting Information). No clear image was obtained for the Bi-YIG film on fused SiO_2, attributed to the transparency of the substrate and film. However, for the film on Si, an increasing out-of-plane magnetic field led to the formation of reverse magnetic domains (white areas) with size on the order of a few μm. Additional images are given in Section S6, and Videos S1 and S2 (Supporting Information) of the magnetization reversal process. The domain size is similar to the grain size (Figure S10, Supporting Information) and the images suggest that increasing

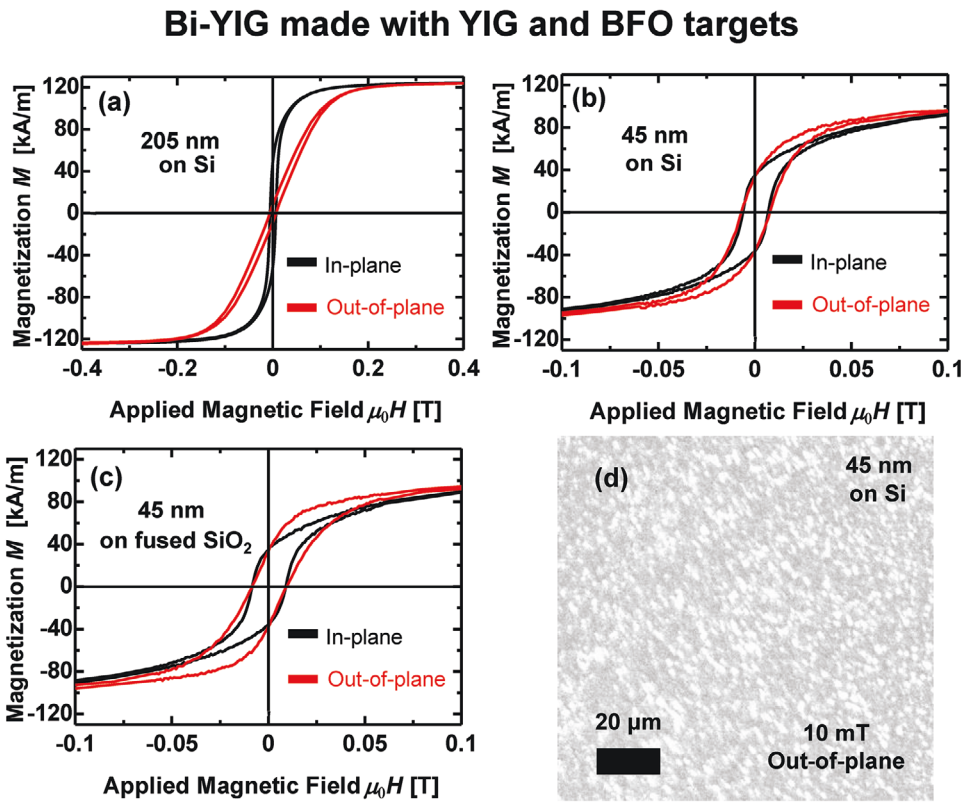

Figure 6. Room temperature in-plane and out-of-plane *M–H* loops of Bi-YIG with Fe deficiency. a) 205 nm thick Bi-YIG film on Si, b) 45 nm thick Bi-YIG films on Si with quench, and c) 45 nm thick Bi-YIG films on fused SiO_2 with quench. d) P-MOKE image of the 45 nm thick Bi-YIG film on Si after saturation followed by a reverse field of 10 mT, close to the coercive field. Light regions indicate the reversal of the out-of-plane magnetization.

the field reverses the grains individually. Since the anisotropy is dominated by the magnetoelastic term, which is orientation dependent, and the grains are randomly oriented, it is likely that the grains have a distribution of anisotropies explaining the wide switching field distribution observed in the MOKE data and the hysteresis loops, and the observed remanence for both in-plane and out-of-plane saturation. The results demonstrate that K_{ME} depends on the Bi%, R value, film thickness, annealing and cooling conditions, and substrate, and that it is possible to induce PMA in Bi-YIG on non-garnet substrates.

2.3. Magneto-Optical and Optical Properties of the Bi-TbIG and Bi-YIG Films

The room temperature FR loops at 1550 nm of the Bi-TbIG and Bi-YIG films, including the 205 nm thick Bi-YIG film with Bi% = 60, are shown in **Figure 7**a,b. The Bi% dependence of the saturation FR for all the films, including the BiIG film, is summarized in Figure 7c. A comparison of the FR and out-of-plane *M–H* loops for the Bi-TbIG and Bi-YIG films is available in Section S7 (Supporting Information), showing a generally good agreement in loop shape and saturation field between the FR and VSM data.

The FR was positive for YIG and TbIG, but adding Bi changed the sign and raised the magnitude of the saturation FR. With increasing Bi%, the FR of the films for Bi% < 50 increased to ≈−1700 deg cm^{-1}, approaching the value obtained for BiIG. Previous studies of Bi-doped IGs[4,7,9,12,13] also showed that the FR at 1550 nm was at most ≈2000 deg cm^{-1}, except for Ref. [14] (6200 deg cm^{-1}) that attributed its high FR to mixed valence cations. For Bi-TbIG and Bi-YIG, the Bi% dependence of saturation FR at 1550 nm is very different from that in the visible region, where the optical parameters (dielectric constant) and saturation FR continue to change until Bi% reaches 100.[39] The similar FR but different M_S of Bi-YIG and Bi-TbIG points to a more complex relationship between FR and M_S. The FR of IGs is not simply proportional to the magnetization but rather depends on the off-diagonal component of permittivity tensor $\epsilon_{ODC}(M)$ that is a function of magnetization, and is generally expressed by $FR = \epsilon_{ODC}\,\omega/2nc$, where ω is the angular frequency, n is the refractive index and c is the speed of light.[3,4]

To investigate the change of dielectric constant with respect to Bi%, the Bi% dependence of n and the extinction coefficient k were measured by ellipsometry, as described in Section S8 (Supporting Information. The ellipsometry yields n at 1550 nm (Figure 7d) and shows that the absorption coefficient α of the films is less than 10 cm^{-1}, i.e., $k < 1.3 \times 10^{-4}$ but a quantitative value below that cannot be obtained by fitting the ellipsometry data. Following the trends seen in FR, n for both the Bi-YIG and Bi-TbIG increases with Bi% up to 50 and varies gradually for higher Bi%. Hence, we have demonstrated that Bi-TbIG with low absorption and a FR comparable to that of epitaxial BiIG (Figure 7c) can be fabricated on a Si substrate.

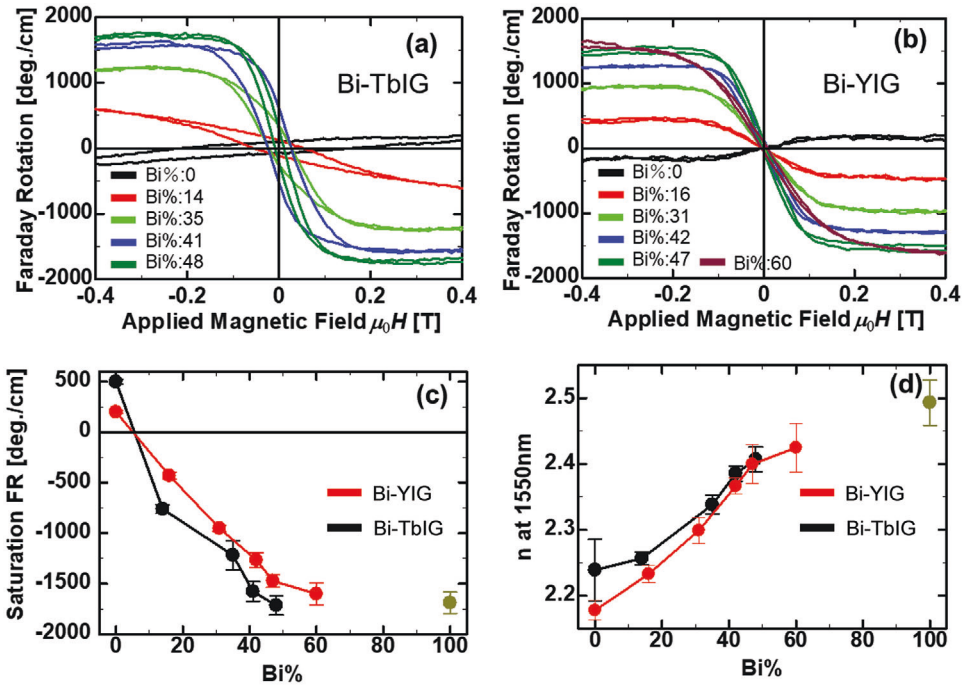

Figure 7. Room temperature FR loops of a) Bi-TbIG and b) Bi-YIG films. Bi% dependence of c) the saturation FR and d) the refractive index n for the Bi-TbIG and Bi-YIG films, where the green data point represents the epitaxial BiIG film.

2.4. Demonstration of Crystallization of Bi-TbIG Using an Integrated Micro-Heater

The prior sections of this article demonstrate magneto-optical Bi-TbIG films via a room temperature (i.e., lift-off-compatible) deposition method without a seed layer, which crystallizes on Si substrates at 873 K, a temperature that can be reached with a doped Si resistive micro-heater. We now demonstrate on-chip crystallization of the Bi-TbIG using the micro-heaters shown in Figure 1. The photoresist was spin coated on a Si chip with an on-chip heater, and the area around the heater was exposed to create a window so that Bi-TbIG could be deposited on the top of the heaters. Then, a Bi-TbIG film with Bi% = 41 was fabricated on the Si chip, and lift-off was performed to pattern the film. The film, initially amorphous, was then annealed by applying a 20 V DC voltage to the micro-heater for 15 s. No visible damage was observed in the on-chip micro-heater after the annealing process.

Figure 8a,b shows an optical microscope image of the Bi-TbIG films before and after annealing on the microheater. A color change is apparent on annealing, with the center of the annealed sample appearing blue. Color changes are seen when using heaters without garnet suggesting the color may come from Si oxidation. Raman measurements at a wavelength of 533 nm for a set of crystallized Bi-TbIG films by RTA and a reference area of the substrate are given in Figure 8c, and at the center of the annealed garnet area in Figure 8d. Crystallized Bi-TbIG films with Bi% above 35 have characteristic peaks ≈470 and 700 cm^{-1} in the Raman spectra, and the same peaks are observed for the Bi-TbIG crystallized on the microheater. While the Raman spectra of Bi-TbIG have not been previously characterized, studies on Bi-YIG[40,41] show that peaks ≈470 and 700 cm^{-1} occur for Bi% = 83 but not for Bi% < 30.

SEM and EBSD measurements (Figure 8e,f) show a polycrystalline film with grain sizes of 2–3 μm, larger than that of the Bi-TbIG in Figure 3 and suggestive of a higher temperature anneal, given the short duration of the microheater anneal (15 s). The film has greater surface roughness and cracking than Figure 3 which may be improved by optimizing the temperature profile of the heater.[30]

3. Conclusion

In this study, Bi-TbIG and Bi-YIG films were grown on Si substrates by PLD at room temperature followed by annealing, and the dependence of their crystallization temperature, magnetic and magneto-optical properties on Bi content and (Bi+Tb or Y):Fe ratio were investigated. Crystallization temperature decreases with increasing Bi content, to 873 K for ≈150 nm thick Bi-TbIG with a 200 s rapid thermal anneal in air. Bi-TbIG with Bi% = 48 has good magneto-optical properties with FR of -1700 deg cm^{-1}, equivalent to that of a single crystal BiIG. The magnetic anisotropy of the films is dominated by shape and magnetoelastic contributions, and the increase in the out-of-plane magnetoelastic anisotropy with Bi content reflects the Bi-dependence of the magnetostriction. Films are under in-plane tensile strain due to thermal expansion mismatch with the substrates, and the strain can be enhanced by growth on a fused SiO_2 substrate due to its lower thermal expansion versus Si. A 45 nm Bi-YIG film with Bi% = 60, which was quenched after crystallization, exhibits perpendicular magnetic anisotropy attributed to the increase in its magnetoelastic anisotropy of 4 kJ m^{-3}. We fabricated Bi-TbIG films on microheaters on Si chips using lift-off processing to pattern the garnet, and demonstrate that they can be crystallized in air by local annealing for 15 s. The results of this

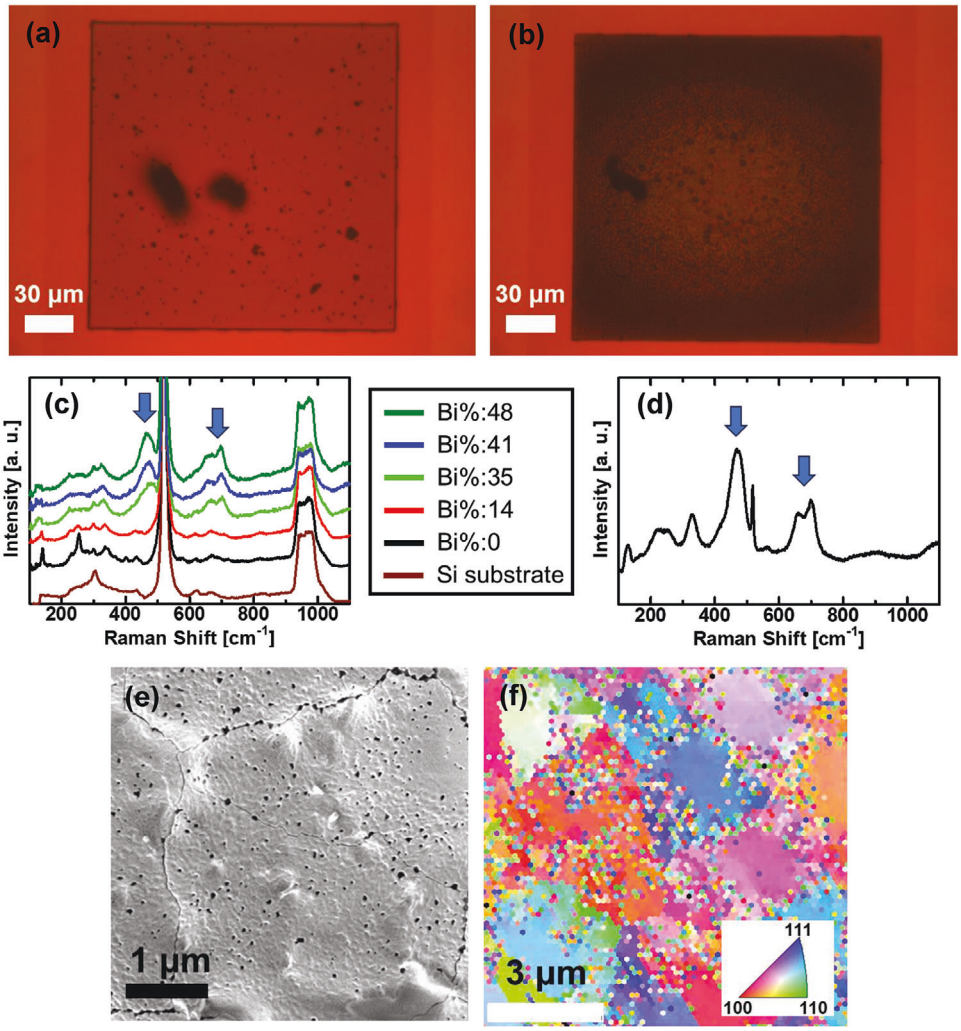

Figure 8. Optical microscope images of Bi-TbIG films on microheaters a) before and a) after on-chip annealing. Raman spectra of the c) Bi-TbIG films on Si substrate in Table 1 and Si substrate and d) Bi-TbIG film on the micro heater. e) SEM image and f) EBSD crystalline orientation mapping of the annealed Bi-TbIG film on the micro-heater.

study provide guidelines for the development of Bi-substituted iron garnet films and their integration with Si devices for silicon photonics and spintronics.

4. Experimental Section

The Bi-TbIG and Bi-YIG films were deposited on (100) double-side polished Si substrates at room temperature by PLD. The Si substrates, which had been cleaned with acetone, isopropanol, and water, were loaded into the PLD chamber (Neocera) and pumped to a base pressure of 5 μTorr, and the oxygen flow rate was adjusted to keep the oxygen partial pressure in the chamber at 10 mTorr. The laser was a KrF excimer laser COMPex Pro 205 from Coherent with a wavelength of 248 nm, irradiating the targets at a frequency of 10 Hz and a fluence of ≈2 J cm^{-2}. Bi-TbIG films were prepared by co-deposition of TbIG and BiIG targets, and the Bi-YIG films were prepared by co-deposition of YIG and BiIG targets. The Bi:Tb or Bi:Y composition (Bi%) was controlled by the number of laser shots applied to each target. The shot ratio for TbIG:BiIG or YIG:BiIG was 60:0, 55:5, 50:10, 45:15, 40:20, and 35:25. Additional Bi-YIG films were made on Si and fused SiO_2 by co-deposition from the YIG target and a BFO target to control the (Bi+Y):Fe composition (R value). The shot ratio was fixed to 40:20 and the thickness of the films was controlled by the number of total laser shots. A BiIG film without Tb and Y was epitaxially grown on a (111) GGG substrate at 833 K as a reference sample. After the deposition, the Bi-TbIG and Bi-YIG films were heated ex situ in the air to crystallize in either an RTA (MILA-5000 from Advance Riko) or a tube furnace. The annealing temperatures are summarized in Table 1. The heating ratio of the RTA and furnace was 15 K s^{-1} and 10 K min^{-1} respectively. While the cooling ratio for the furnace was 1 K min^{-1}, that for RTA was 10 K s^{-1} above 773 K, 1–2 K s^{-1} for 573–773 K, and <1 K s^{-1} for below 573 K. Some of the films heated with the furnace were quenched by removing the films out of the hot furnace and putting them on a large aluminum plate, leading to a cooling rate of ≈100 K s^{-1}.

The crystal structures of the Bi-TbIG and Bi-YIG films were identified by X-ray diffraction (XRD, X'pert Pro MPD from Malvern Panalytical (45 kV and 40 mA) and Rigaku SmartLab (45 kV and 200 mA)) with Cu-Kα radiation. The thickness of the films was measured by profilometry (Veeco Dektak 150) and X-ray reflectometry (Bruker D8 High-Resolution XRD), and the sample composition was determined by wavelength dispersive spectrometry on an electron probe microanalyzer (JEOL JXA-8200 Superprobe, at 15 kV and 10 nA). The cation composition, film thickness, and annealing temperature of all the samples are summarized in Table 1. In

the first column, the cation composition of the formula unit is normalized such that Fe = 5. Since some Bi-YIG films fabricated from the YIG and BFO targets have a low film thickness, which impedes composition analysis using WDS, the cation composition for the 205 nm thick one was taken as the composition of those Bi-YIG series. Bi content is defined as $Bi\% = \{Bi/(Bi + Tb)\} \times 100$ or $Bi\% = \{Bi/(Bi + Y)\} \times 100$ for the Bi-TbIG and Bi-YIG films respectively. Moreover, the R value is defined as $R = \{(Bi + Tb)/Fe\}$ or $R = \{(Bi + Y)/Fe\}$. The surface topography of the samples was measured using atomic force microscopy (AFM, Oxford Instruments Cypher), and the orientation distribution and size of the grains was measured by electron backscatter diffractometry (EBSD, Zeiss Merlin high-resolution scanning electron microscope). The *M–H* loops of the samples were investigated by vibrating sample magnetometry (VSM, ADE Technologies Model 1660) at room temperature for fields in-plane or out-of-plane to the film plane. For the Bi-TbIG films, in-plane *M–H* loops were also measured from 123 to 298 K, and the temperature at which $M_S = \approx 0$ was taken as the compensation temperature $T_{comp.}$ The P-MOKE images were obtained with a polarizing microscope equipped with an electromagnet, using light from a LED with a wavelength of 467 nm. Before taking P-MOKE images, a magnetic field of ±60 mT was applied in out-of-plane direction and removed, and the image at 0 mT was used as the reference image and subtracted from each image. After that, images were acquired up to ∓ 60 mT. The FR of the samples was measured by passing polarized light at a wavelength of 1550 nm (Thorlabs LDM1550 laser) perpendicularly through the sample and measuring the light transmitted through an analyzer using a Ge photodetector as a function of field perpendicular to the sample. The positive FR of Si was subtracted by fitting a parabolic background. The refractive index *n* and optical loss of the samples were estimated by ellipsometry (Semilab SE-2000 spectroscopic ellipsometer).

The micro heaters on the chip have the structure shown in Figure 1 and a size of 250 µm square. A window of 200 um square was made in a photoresist layer by maskless optical lithography and a Bi-TbIG film with Bi% = 41 was deposited on it at room temperature. After lift-off, the garnet film was annealed by applying a 20 V DC voltage to the micro heater for 15 s. The crystal structure of the Bi-TbIG film was identified by Raman spectroscopy (Renishaw Invia Reflex Micro Raman with laser wavelength of 533 nm).

Supporting Information

Supporting Information is available from the Wiley Online Library or from the author.

Acknowledgements

The authors acknowledge support from NSF award ECCS 2028199 and ECCS 2328839 and from Fujikura. Shared facilities of MIT Characterization.nano were used for this work. K.H. was supported by JSPS KAKENHI grant numbers 20J12063 and 22KJ3113.

Conflict of Interest

The authors declare no conflict of interest.

Data Availability Statement

The data that support the findings of this study are available from the corresponding author upon reasonable request.

Keywords

garnet oxides, local annealing, magneto-optical garnets, on-chip crystallization, perpendicular magnetic anisotropy

Received: March 13, 2024
Revised: April 29, 2024
Published online:

[1] B. Jalali, S. Fathpour, *J. Light. Technol.* **2006**, *24*, 4600.
[2] S. Y. Siew, B. Li, F. Gao, H. Y. Zheng, W. Zhang, P. Guo, S. W. Xie, A. Song, B. Dong, L. W. Luo, C. Li, X. Luo, *J. Light. Technol.* **2021**, *39*, 4374.
[3] S. Kharratian, H. Urey, M. C. Onbashı, *Adv. Optical Mater.* **2020**, *8*, 1901381.
[4] K. Srinivasan, B. J. H. Stadler, *Opt. Mater. Express* **2022**, *12*, 697.
[5] L. Bi, J. Hu, P. Jiang, D. H. Kim, G. F. Dionne, L. C. Kimerling, C. A. Ross, *Net. Photon.* **2011**, *5*, 758.
[6] Y. Shoji, T. Mizumoto, *Sci. Technol. Adv. Mater.* **2014**, *15*, 014602.
[7] P. Dulal, A. D. Block, T. E. Gage, H. A. Haldren, S. Y. Sung, D. C. Hutchings, B. J. H. Stadler, *ACS Photonics* **2016**, *3*, 1818.
[8] P. Pintus, D. Huang, C. Zhang, Y. Shoji, T. Mizumoto, J. E. Bowers, *J. Light. Technol.* **2017**, *35*, 1429.
[9] T. Fakhrul, S. Tazlaru, L. Beran, Y. Zhang, M. Veis, C. A. Ross, *Adv. Optical Mater.* **2019**, *7*, 1900056.
[10] K. Srinivasan, C. Zhang, P. Dulal, C. Radu, T. E. Gage, D. C. Hutchings, B. J. H. Stadler, *ACS Photonics* **2019**, *6*, 2455.
[11] S. Chikazumi, *Physics of Ferromagnetism*, Oxford University Press, Oxford, UK **1997**
[12] S. Higuchi, Y. Furukawa, S. Takekawa, O. Kamada, K. Kitamura, K. Uyeda, *Sens. Actuator A Phys.* **2003**, *105*, 293.
[13] A. D. Block, P. Dulal, B. J. H. Stadler, N. C. A. Seaton, *IEEE Photonics J* **2014**, *6*, 1.
[14] T. Fakhrul, S. Tazlaru, B. Khurana, L. Beran, J. Bauer, M. Vančík, A. Marchese, E. Tsotsos, M. Kučera, Y. Zhang, M. Veis, C. A. Ross, *Adv. Optical Mater.* **2021**, *9*, 2100512.
[15] K. Srinivasan, C. Radu, D. Bilardello, P. Solheid, B. J. H. Stadler, *Adv. Funct. Mater.* **2020**, *30*, 2000409.
[16] K. Matsumoto, K. Yamaguchi, T. Fuji, A. Ueno, *J. Appl. Phys.* **1991**, *69*, 5918.
[17] H. Zhao, J. Zhou, B. Li, Z. Gui, L. Li, *J. Electroceram.* **2008**, *21*, 802.
[18] H. Lee, Y. Yoon, H. Yoo, S. A. Choi, K. Kim, Y. Choi, H. Melikyan, T. Ishibashi, B. Friedman, K. Lee, *J. Alloys Compd.* **2011**, *509*, 9434.
[19] M. J. Gross, J. J. Bauer, S. Ghosh, S. Kundu, K. Hayashi, E. R. Rosenberg, K. A. Mkhoyan, C. A. Ross, *J. Magn. Magn. Mater.* **2022**, *564*, 170043.
[20] J. J. Bauer, E. R. Rosenberg, C. A. Ross, *Appl. Phys. Lett.* **2019**, *114*, 052403.
[21] J. J. Bauer, E. R. Rosenberg, S. Kundu, K. A. Mkhoyan, P. Quarterman, A. J. Grutter, B. J. Kirby, J. A. Borchers, C. A. Ross, *Adv. Electron. Mater.* **2020**, *6*, 1900820.
[22] S. Sedky, A. Witvrouw, H. Bender, K. Baert, *IEEE Trans. Electron Devices* **2001**, *48*, 2.
[23] Y. L. Cheng, Y. L. Lin, C. Y. Lee, G. S. Chen, *J. S. Fang* **2019**, *24*, 3882.
[24] Y. Suzuki, T. Goto, Y. Eto, H. Takagi, P. Boey, L. Alexander, V. Baryshev, M. Inoue, *J. Magn. Soc. Jap.* **2012**, *36*, 183.
[25] Y. Sgibnev, A. Shelaev, D. Kulikova, A. Salatov, P. Tananaev, G. Yankovskii, A. Baryshev, *Growth Des* **2022**, *22*, 1196.
[26] L. Soumah, N. Beaulieu, L. Qassym, C. Carrétéro, E. Jacquet, R. Lebourgeois, J. B. Youssef, P. Bortolotti, V. Cros, V. Cros, A. Anane, *Nat. Commun.* **2018**, *9*, 3355.
[27] L. Caretta, S. H. Oh, T. Fakhrul, D. K. Lee, B. H. Lee, S. K. Kim, C. A. Ross, K. J. Lee, G. S. D. Beach, *Science* **2020**, *370*, 1438.
[28] P. Hansen, K. Witter, W. Tolksdorf, *Phys. Rev. B* **1983**, *27*, 6608.
[29] M. J. Gross, W. A. Misba, K. Hayashi, D. Bhattacharya, D. B. Gopman, J. Atulasimha, C. A. Ross, *Appl. Phys. Lett.* **2022**, *121*, 252401.
[30] Y. Zhang, C. Fowler, J. Liang, B. Azhar, M. Y. Shalaginov, S. D. Jones, S. An, J. B. Chou, C. M. Roberts, V. Liberman, M. Kang, C. Ríos, K. A.

Richardson, C. R. Baleine, T. Gu, H. Zhang, J. Hu, *Nat. Nanotechnol.* **2021**, *16*, 661.
[31] M. Y. Chern, J. S. Liaw, *Jpn. J. Appl. Phys.* **1997**, *36*, 1049.
[32] I. Nadinov, O. Kovalenko, J. L. Rehspringer, M. Vomir, L. Mager, *Ceram. Int.* **2019**, *45*, 21409.
[33] R. Hock, H. Fuess, T. Vogt, M. Bonnet, *J. Solid State Chem.* **1990**, *84*, 39.
[34] M. C. Morris, H. F. McMurdie, E. H. Evans, B. Paretzkin, H. S. Parker, N. C. Panagiotopoulos, C. R. Hubbard, "Standard X-ray Diffraction Powder Patterns Section 18" National Bureau of Standards Department of Commerce (National Institute of Standards and Technology) **1981**.
[35] V. J. Fratello, S. J. Licht, C. D. Brandle, H. M. O'Bryan, F. A. Baiocchi, *J. Cryst. Growth* **1994**, *142*, 93.
[36] H. Watanabe, N. Yamada, M. Okaji, *Int. J. Thermophys.* **2004**, *25*, 221.
[37] J. Oishi, T. Kimura, *Metrologia* **1969**, *5*, 50.
[38] S. Iida, *J. Phys. Soc. Jpn.* **1967**, *22*, 1201.
[39] E. Jesenska, T. Yoshida, K. Shinozaki, T. Ishibashi, L. Beran, M. Zahradnik, R. Antos, M. Kučera, M. Veis, *Opt. Mater. Express* **2016**, *6*, 1986.
[40] T. Okuda, N. Koshizuka, K. Hayashi, T. Takahashi, H. Kotani, H. Yamamoto, *J. Magn. Soc. Jap.* **1987**, *11*, 179.
[41] A. Raja, P. M. M. Gazzali, G. Chandrasekaran, *Physica B* **2021**, *613*, 412988.